# Impacts of 2020 Beirut Explosion on Port Infrastructure and Nearby Buildings

Salah Sadek, M.ASCE[1]; Mayssa Dabaghi, A.M.ASCE[2]; Timothy M. O'Donnell, S.M.ASCE[3]; Paolo Zimmaro, M.ASCE[4]; Youssef M. A. Hashash, F.ASCE[5]; and Jonathan P. Stewart, F.ASCE[6]



**Abstract:** At 18:08 on August 4, 2020, a large explosion occurred at Hangar 12 in the Port of Beirut. The size of the explosion was equivalent to that of an earthquake with a local magnitude ($M_L$) of 3.3 according to the USGS. As one of the largest nonmilitary explosions to ever impact an urban region, this event provides unprecedented opportunities to document explosion impacts on urban infrastructure. To facilitate this data collection, the Geotechnical Extreme Events Reconnaissance (GEER) Association coordinated a multiagency response directed toward the collection of perishable data of engineering interest. Two main categories of infrastructure systems were impacted: the Port of Beirut and the Beirut building stock. Within the Port, the explosion triggered a quay wall failure and flow slide, and strongly impacted grain silo structures that were in close proximity to Hangar 12. Within the city, historical masonry structures, older reinforced concrete structures, and modern high-rise structures were impacted. Through a combination of in-person inspections and street-view surveys, we collected data on structural performance (including damage to load-bearing elements) and building façades. Performance levels were classified according to procedures applied following earthquakes (for structural performance) and newly proposed procedures (for façades). We describe spatial distributions of these damage types and dependencies on source distance and location-to-explosion direction. We demonstrate that physical damages correlated with damage proxy maps produced by the Jet Propulsion Laboratory and the Earth Observatory of Singapore based on Copernicus Sentinel-1 satellite synthetic aperture radar data, with a stronger correlation with structural damage than with façade damage. **DOI: 10.1061/(ASCE)NH.1527-6996.0000550.** 

## Introduction

At 18:08 on August 4, 2020, a large explosion occurred at Hangar 12 in the Port of Beirut, Lebanon, at a facility storing ammonium nitrate. The death toll from the blast was at least 220, with injuries on the order of 7,000. Hundreds of those injured were left with considerable and permanent scars and long-term impairments. An estimated 300,000 people lost their homes and needed immediate temporary shelter. The direct damages to structures, infrastructure, and other facilities were estimated at about US$4 billion, with direct economic losses on the order of US$3 billion (World Bank Group 2020).

A number of technical topics have been investigated in connection with this event, including the blast yield [around 0.50-kt TNT (Rigby et al. 2020; Diaz 2020; Aouad et al. 2020; Pilger et al. 2021)], generated seismic waves (Nemer 2021), simulations of air pressure (blast) waves (Valsamos et al. 2021; Zhang et al. 2021), structural response of the Beirut silos (Temsah et al. 2021; Ismail et al. 2021), trauma experienced by people impacted by the blast (Al-Hajj et al. 2021), and risk/consequence analyses of the event (Yu et al. 2021). Whereas the Beirut event presents a number of unique features related to scope and context, the nature of the blast and its magnitude are comparable to the Toulouse AZF plant explosion of 2001 (Dechy et al. 2004).

In this article, we describe the impacts of the blast on physical infrastructure, based on reconnaissance coordinated by the Geotechnical Extreme Events Reconnaissance (GEER) association in collaboration with multiple government and university entities in Beirut. In addition to the GEER response, a number of local and international agencies conducted immediate relief and assessment work (Beirut OEA 2020; LRC 2020; Dar Group 2020; Search and Rescue Assistance in Disasters, SARAID 2020); when available to us, the data from those additional studies were used as part of the present work.

In this paper, we focus on two main effects of the event:

- The near-field impact of the explosion on Port of Beirut infrastructure, including apparent foundation deformations of the grain silos and failure of a quay wall with flow failure of retained artificial fill.
- The spatially variable impacts of the explosion on buildings in Beirut. We document distributions of structural damage

[1]Professor, Maroun Semaan Faculty of Engineering and Architecture, American Univ. of Beirut, Beirut 1107 2020, Lebanon. ORCID: https://orcid.org/0000-0002-0672-8305

[2]Assistant Professor, Maroun Semaan Faculty of Engineering and Architecture, American Univ. of Beirut, Beirut 1107 2020, Lebanon. ORCID: https://orcid.org/0000-0003-2017-3462

[3]Graduate Student Researcher, Dept. of Civil and Environmental Engineering, Univ. of California, Los Angeles, CA 90095.

[4]Assistant Professor, Dept. of Environmental Engineering, Univ. of Calabria, 87036 Arcavacata di Rende, 87036, Italy; Visiting Project Scientist, Dept. of Civil and Environmental Engineering, Univ. of California, Los Angeles, CA 90095. ORCID: https://orcid.org/0000-0002-3544-5961

[5]Professor, Dept. of Civil and Environmental Engineering, Univ. of Illinois, Urbana–Champaign, IL 61801.

[6]Professor, Dept. of Civil and Environmental Engineering, Univ. of California, Los Angeles, CA 90095 (corresponding author). ORCID: https://orcid.org/0000-0003-3602-3629. Email: jstewart@seas.ucla.edu

Note. This manuscript was submitted on July 22, 2021; approved on November 22, 2021; published online on March 2, 2022. Discussion period open until August 2, 2022; separate discussions must be submitted for individual papers. This paper is part of the ***Natural Hazards Review***, © ASCE, ISSN 1527-6988.

(i.e., affecting load-bearing elements) and exterior (façade) damage to building openings such as windows and doors.

Subsequent sections describe information sources and data collection, the explosion impacts in the Port of Beirut, and the explosion impacts on buildings in Beirut. The paper concludes with a summary and description of how the information compiled in this work can be useful in future research. Additional information on the reconnaissance is provided in a GEER report (Sadek et al. 2021a). All data collected as part of this study are available on DesignSafe (Rathje et al. 2017) as a published data set (Sadek et al. 2021b).

## Information Sources and Data Collection

### GIS Database

We used a geographic information system (GIS) database for Beirut created by the American University of Beirut Beirut Urban Lab (AUB-BUL). The database includes cadastral information as well as building, road, population, and other related data. For buildings, the AUB-BUL GIS map includes location, approximate size, and date of construction. This information was derived from public sources, such as cadastral and assessor files at the Lebanese Ministry of Finance. Buildings in the AUB-BUL inventory are shown in Fig. 1 (shading is based on OEA surveys described further below).

Open Map Lebanon is a community-based endeavor formed after the August 4 blast to promote data dissemination and relief efforts. One of the tasks it undertook was street-level imagery compiled using Mapillary. A large fraction of the images available on the Open Map Lebanon Mapillary application were contributed by Sadek et al. (2021b).

### Order of Engineers and Architects Surveys

On August 12, 2020, the Beirut Order of Engineers and Architects (OEA) launched a large-scale field survey in the areas closest to and most affected by the blast, as illustrated in Fig. 1. This effort was led by the OEA Public Safety Committee and used approximately 1,000 volunteers of various specialties. A total of 3,040 properties containing 2,509 buildings were inspected in the designated area. The OEA generated weekly structural damage summary reports and a final report (OEA 2020) and established a central data bank in which collected images and team reports were filed. Full access to this data remains pending.

The OEA documented the condition of the buildings they surveyed and provided building-specific recommendations of evacuation, closure, or strengthening (full or partial, immediately or during repair) for the most damaged buildings. As shown in Fig. 1, the damage was classified as no damage, cracks in building components, damage to nonstructural components, and risk of full/partial collapse. Relative to the blast site, the OEA inspections occurred in a range of up to 1 km west, 1 km south, and 1.5 km east, in the districts of Minet El-Hosn, Zokak El Blat, Port, Saifi, Rmeil, and Medawar. At the southern limit of the inspection areas, damage levels of "no/minor damage" were recorded, whereas appreciable damage was observed at the western and eastern limits, suggesting that damage locations may have extended beyond the range of the OEA surveys. The OEA damage assessments shown in Fig. 1 were obtained from the OEA's report (OEA 2020). Data from the most heavily damaged buildings inspected by the OEA have been incorporated here, as described in more detail in the section "Building Impacts."

### Dar Group Surveys

The Dar Group is an engineering consulting firm based in Beirut. On behalf of the Beirut municipality, its members performed street surveys of about 7,000 buildings from August 11 to September 10, 2020, for the Beirut Municipality (Dar Group 2020). These surveys evaluated and photographed buildings from street level (structures were generally not entered). The objective was to determine the extent of structural damage sustained by buildings (no damage, partial collapse, or total collapse) in order to classify them as safe (green), restricted use (yellow), or unsafe (red) for occupants. The investigation also included an assessment of the extent of façade damages in terms of estimated quantities of damaged glazing and cladding.

The Dar Group surveyed a wider geographic area than did the OEA and included buildings in the districts of the Port, Achrafieh, Rmeil, Medawar, Mousseitbeh, Mazraa, Ain Mreisseh, and Ras Beirut. Field reports along with images of the surveyed properties were obtained from Dar and integrated into the central database at the Beirut Urban Lab. This information was analyzed in reference to identifiable damage categories. It was not incorporated here because the definitions of the structural damage categories used by DAR differed from ours and thus required further investigation

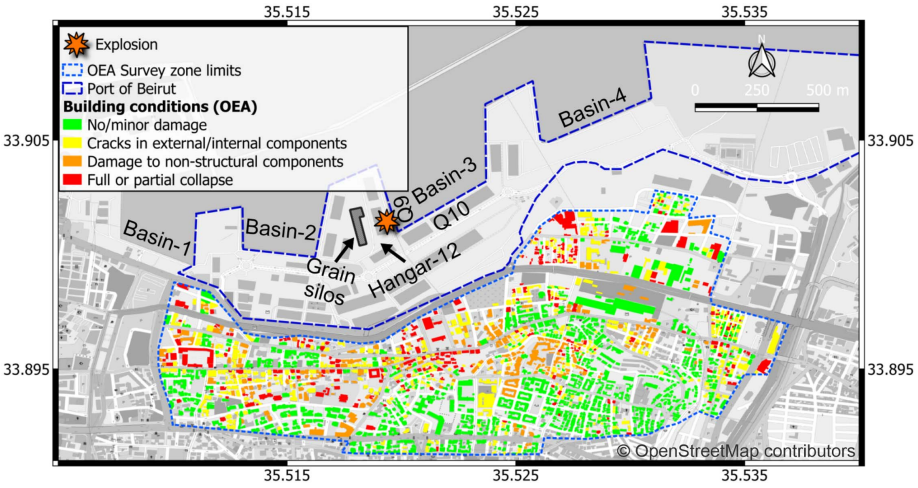


**Fig. 1.** Map of Beirut showing location of explosion, Port of Beirut, and condition of buildings surveyed by the OEA; basin and quay wall numbers are provided for the port. (Data from OEA 2020; Base map © OpenStreetMap contributors.)

for consistent damage classification. The façade damage data collected by DAR may be incorporated in future studies.

### Lebanese Red Cross

In addition to the treatment and transport of the wounded and providing help in the evacuation of damaged hospitals, the Lebanese Red Cross (LRC) performed about 50,000 door-to-door household needs assessments, and provided direct cash assistance to about 10,000 vulnerable affected families for basic needs and urgent repairs. The LRC assessments included a shelter condition assessment that consisted of observations of structural damage and damage to windows and external doors (LRC 2020). Access to these data remains pending.

### GEER Association Reconnaissance

The GEER Association formed a reconnaissance team in August 2020 to examine the engineering impacts of the explosion with the aim of collecting and documenting perishable data. The emphasis of the collection was on impacts in the Port and in the city building stock, as noted in the Introduction. The data collection involved in-person reconnaissance and street-view surveys, as described subsequently. In addition, we incorporated data from OEA (2020) for the interpretation of structural damage patterns.

## Port Infrastructure Impacts

### Port Facility

Beirut is one of the oldest cities in the world, continuously inhabited for more than 5,000 years. The city's coastline and safe water harbor/port(s) have shifted westward and northward over various periods of expansion and reclamation. The Port of Beirut has seen periods of growth and change in function/role over the various eras. During the Roman presence (64 BCE to the middle of the 6th century CE), it was a commercial and economic center serving the "colonies." This was followed by the Omayyad, Crusaders, and Mameluke periods, in which the Port was the berth of armed fleets; later it served as a hub for pilgrims visiting the Holy Lands.

The "modern" incarnation of the Beirut Port leading to its present extent started in the late 19th century, when a concession was given by the Ottoman authorities to a private company to expand and manage the facility. Following World War I, under the French Mandate for Syria and Lebanon (i.e., a period of French oversight of local governance), the Port management company was reorganized and granted a new concession in 1925 that ended in 1960. From 1960 to 1990, a Lebanese company operated the Port, after which it was returned to the state. Fig. 2 shows the significant expansions of the Port facilities that were made since 1875, including the number and size of docks, deeper drafts, and larger commercial and storage areas.

In the past 30 years, additional, more significant expansions of the Port were completed. These allowed for a large container facility and larger and deeper water docks, allowing the facility to receive the largest container/cargo vessels. As of 2019, the Beirut Port accounted for more than 60% of Lebanon's total imports (*New York Times* 2020) valued at roughly 25% of GDP. Fig. 1 depicts the Port facility with its various basins and quays as it was before 4 August 2020.

Given the original footprint and sequence of expansion of the Port over time, methods of construction and associated complexities were multiple and varied. In its earliest versions, the Port was located in a natural "deepwater" bay along a rocky portion of the shoreline. The earliest protective seawalls were built by dumping rock sourced from limestone quarries in the foothills closest to the shore. More modern expansions up to the 1950s (Fig. 1, Basins 2 and 3) relied on concrete blocks to form quay walls with miscellaneous backfill to form the docks behind the newly established quays. As the Port expanded further east, particularly for Basin 4 and the newest deepwater quays facing north, large-diameter driven piles were used to form the foundation of the walls and dock slabs, particularly in the zone of operation of the container cranes and handling equipment. The use of such foundations was accompanied by ground improvement in the general dock areas in the container terminal. These consisted of preloading with wick drains placed in the seabed sediments in some locations along with complementary dynamic compaction of the granular fill.

In the mid- to late 1960s, plans were drawn and executed to build the largest grain storage facilities of their kind in the region. Phase I of the project consisted of 8 silo columns 3 rows deep. Phase II, completed in 1969, extended the facility to 14 silo columns 3 rows deep with a total capacity of 105,000 t of grain (Fig. 3). The Beirut Port silos were considered a feat of engineering at the time. As shown in Fig. 4, they consisted of 3 parallel rows of 14 cylindrical concrete silos, supported on 2,900 driven precast reinforced concrete piles 12–15 m deep. Phase III saw the addition of 6 cells, raising the total number of columns to 16 and the capacity to 150,000 t. Fig. 5 shows a soil profile at the site based on data from boreholes drilled at the time of planning for Phase 1 and provided by Forex Sarl (a local site exploration company). Overburden-corrected standard penetration test (SPT) data are shown for the approximately 13-m-deep fill layer at this location. The average value of 20 blows/0.3 m ($N_1 = 20$ blow/ft); the energy level is unknown but is estimated as 45%–60%.

In the late 1990s, a structural assessment was conducted on the silos. Significant deterioration of the 17–18-cm-thick outer concrete silo shells was observed, mostly due to exposure to the humid

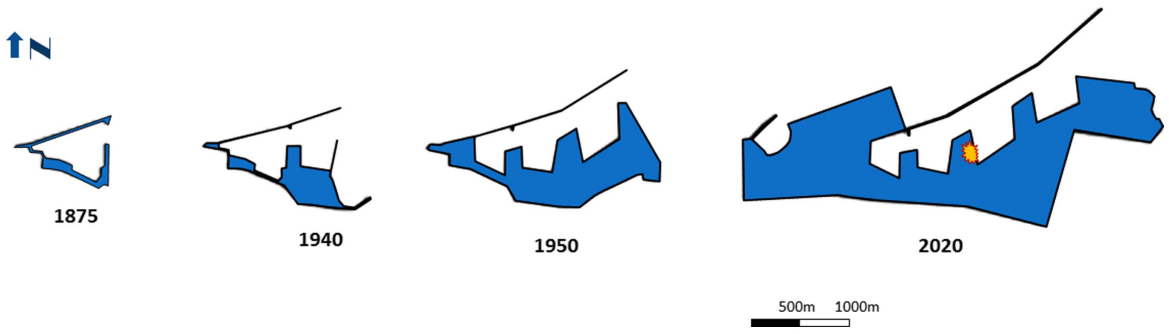


**Fig. 2.** Scaled representation of Beirut Port expansion from 1875 to 2020. Explosion location marked in 2020 map.



Nat. Hazards Rev., 2022, 23(2): 04022008

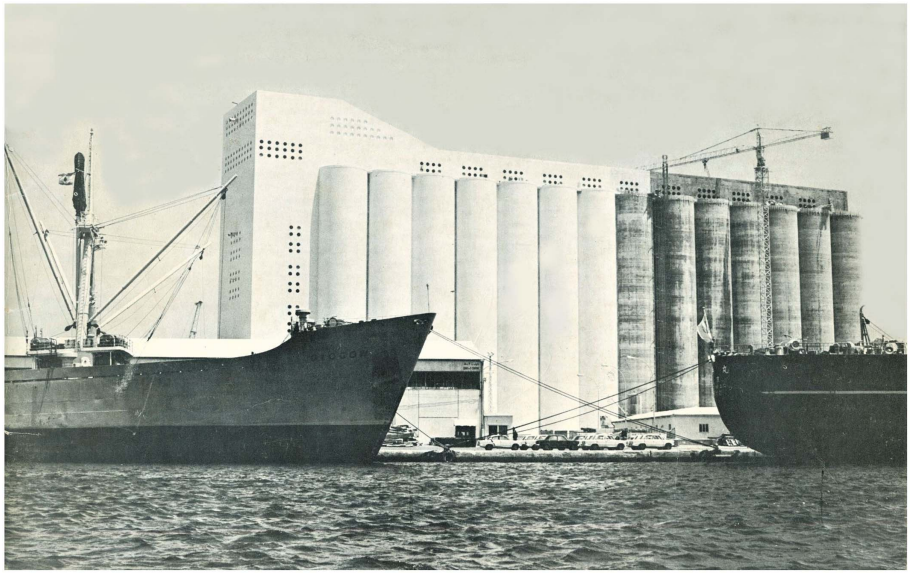

**Fig. 3.** Phase-I grain silos completed and Phase-II silos nearing completion. (Reprinted from Ministry of Public Works and Transport 1970.)

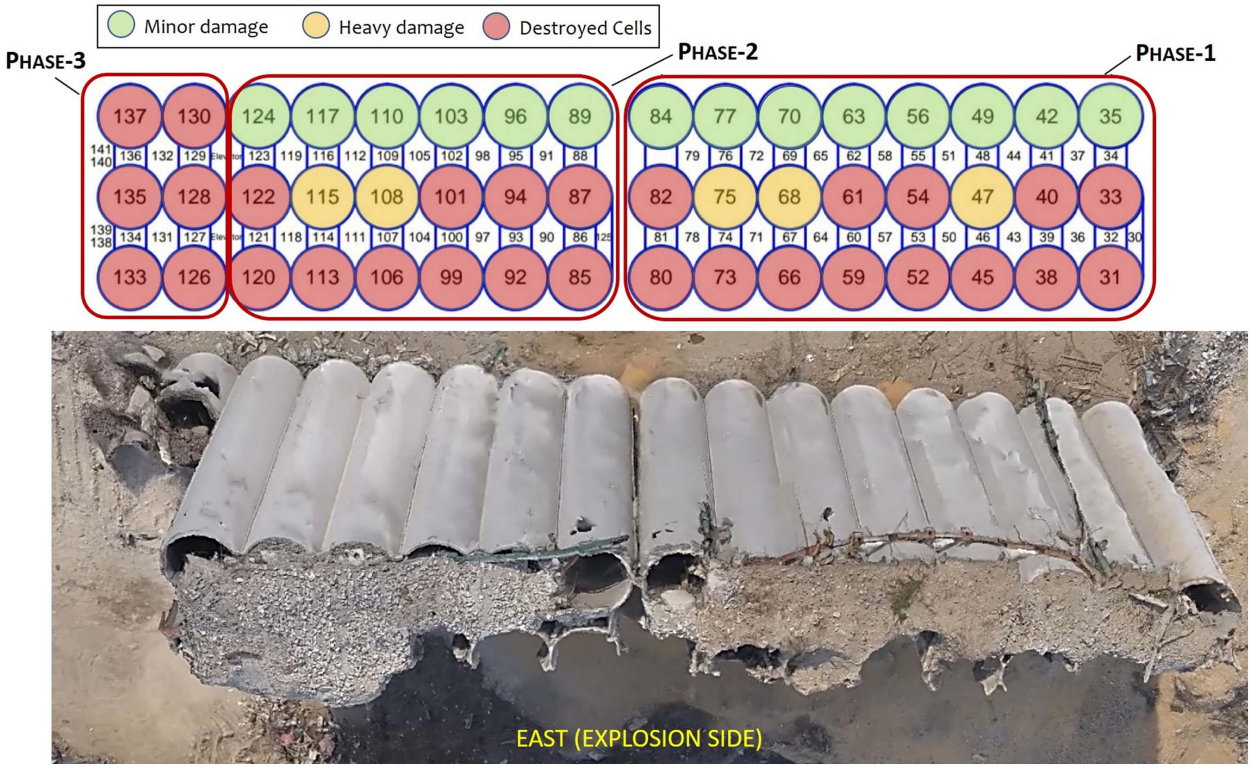


**Fig. 4.** Plan view showing configuration of grain silo complex. Silo shading indicates blast damage levels. Photo is a composite aerial imagery with laser scan survey looking down. (Image courtesy of E. Durand.)

and salty seafront environment and subsequent carbonation. The damage was addressed by constructing a 12-cm-thick reinforced concrete jacket on the inner walls of the outer/exposed silos. This strengthening measure improved the silos' response to the blast on August 4, 2020.

### *Impacts on Grain Silos*

When combined, the Beirut Port grain silos made up a substantial structure, roughly 175 m long and 30 m wide, with a height of 50 m. Parts of the silos were full or partially full with grain at the time of the event, increasing the mass and bulk resistance of the thin concrete shell cylinders.

Fig. 6 shows the extensive damage to the silos from the explosion, which was as close as 50 m. The silos visible in the photograph are from the second and third rows because the first (easternmost) row of silos was completely destroyed. Near the base of the silos in Fig. 6 is spilled grain. The specific condition of each silo after the blast, shown in Fig. 4, fell into three categories: intact, heavily damaged, and destroyed. The explosion exposed the gap at

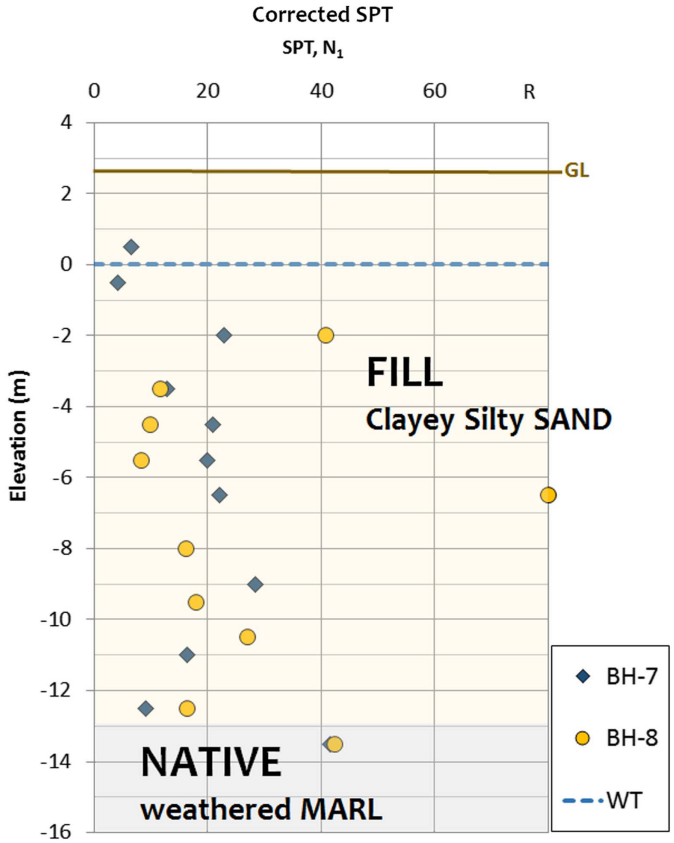


**Fig. 5.** Subsurface profile; data taken from boreholes below footprint of Phase-1 silos. (Data courtesy of Forex Sarl.)

the construction joint between the Phase-I and Phase-II silos, which is visible in Fig. 6. The gap does not appear to have widened as a result of the blast. Most cells were partially filled at the time of the explosion, except for the six southernmost cells (126 to 137 in Fig. 4). Along the west-facing third-row of cells, those that were partially filled survived whereas those that were empty (at the south end) were completely lost.

Multi-epoch LiDAR scans of the silos were performed on September 17, 2020, November 23, 2020, and March 28, 2021, by Mr. Emanuel Durand of Amann Engineering. These scans allowed the tilt of the surviving silos to be assessed. Fig. 7 shows orthometric views of the west side of the silos from the September 17 scan, with shading indicating horizontal displacement relative to a vertical plane. The results from this initial scan show a consistent tilt westward (away from the blast) on the order of 25 cm. Scans taken on November 23 do not indicate any additional movement. As shown in Fig. 8, in the time between November and the last scan taken on March 27, 2021, movement toward the east had occurred, mainly involving silos that are part of the Northern block (Silos 35 to 82 in Fig. 4). Representative deviations from vertical for Silos 49 and 77 are shown in Fig. 9. The reversal/recovery of the tilt may be attributed to heavy rainfall causing further erosion and expansion of the crater at the blast epicenter, combined with gradual creep effects at the foundation level because the piles supporting the silos and/or connecting caps likely had been sheared and/or damaged.

### *Crater and Quay Wall 9 Flow Slide*

The blast at Hangar 12 left a crater nearly 120 m in diameter. Fig. 10 shows before and after aerial views of Hangar 12 and the crater. In the aftermath of the event, detailed bathymetric surveys were conducted by teams from the Lebanese army using boat-mounted bottom profilers, which provide water depths to ~1-cm resolution. The nominal preexplosion depth in Basin 3 was 10.5 m (this depth was maintained to accommodate the needs of cargo ships serviced by the Port). Fig. 11(a) shows the postevent depth contours four days after the blast, and Fig. 11(b) shows a west-east cross section through the crater.

The geometry and size of the crater clearly correspond to the blast location (Hangar 12). The crater is 120 m in diameter and roughly 4.5 to 5 m deep; the depth would likely have been greater had it not been for the presence of water at ~0-m elevation. Volume calculations were conducted on the 3D crater and the debris that


**Fig. 6.** View from the east of silos following blast; picture taken from Quay 10 (33°54′6.35″N; 35°31′16.19″E). (Image reprinted from Sadek et al. 2021a.)

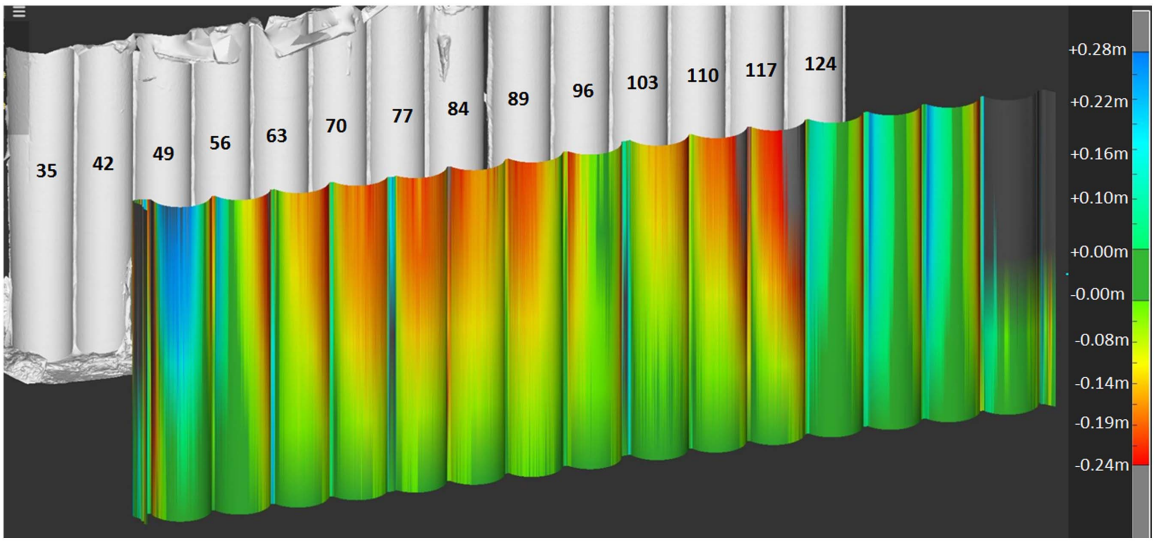


**Fig. 7.** Horizontal deflections of west side of silos as evaluated from LiDAR point cloud data; horizontal deflections indicate consistent tilt away from blast at top of multiple silos with maximum around 24 cm on September 17, 2020 (negative values indicate movement westward from blast epicenter). (Reprinted from Sadek et al. 2021a.)

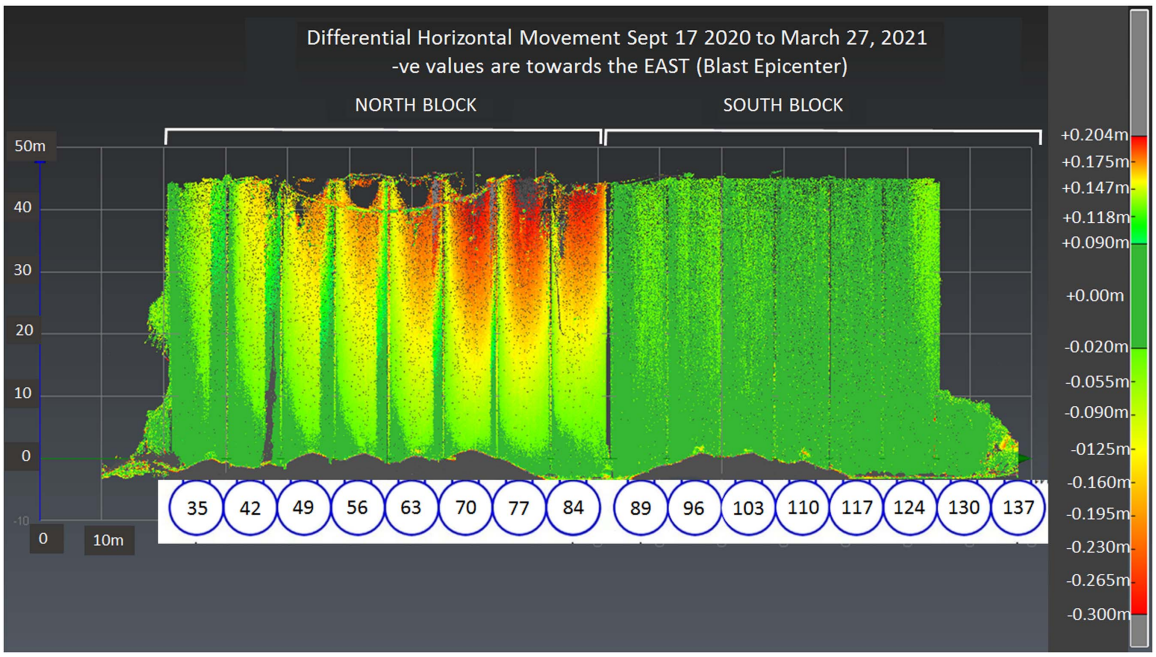


**Fig. 8.** Point cloud data shaded with reference to differential horizontal movement between September 17, 2020 (first postblast readings) and March 27, 2021; negative values indicate eastward movement toward blast epicenter. (Base scans courtesy of Amann Engineering.)

flowed out into the basin (Sadek et al. 2021a). These calculations showed that the volume of material displaced into the basin was roughly 38,500 $m^3$, compared to 45,500-$m^3$ volume of material lost from behind the original location of the quay wall. The "missing" balance of ~7,000 $m^3$ was likely fill material behind the quay wall and above the water level that was ejected into the air and deposited away from the blast zone. These numbers confirm the likelihood that the material retained by the quay wall flowed/ran out into the basin for a considerable distance, as shown in Fig. 11(b) (on the order of 80 m).

## Building Impacts

Beirut has a rich architectural history and contains buildings spanning many construction eras. Structures built before the 1950s–1960s were typically low-rise stone masonry bearing wall buildings developed without adherence to modern building codes. Several of these structures that have architectural or historical value are classified as heritage buildings by the Ministry of Culture's Directorate General of Antiquities (DGA). Mid-rise reinforced concrete frame structures emerged in the 1950s. During the Lebanese civil war

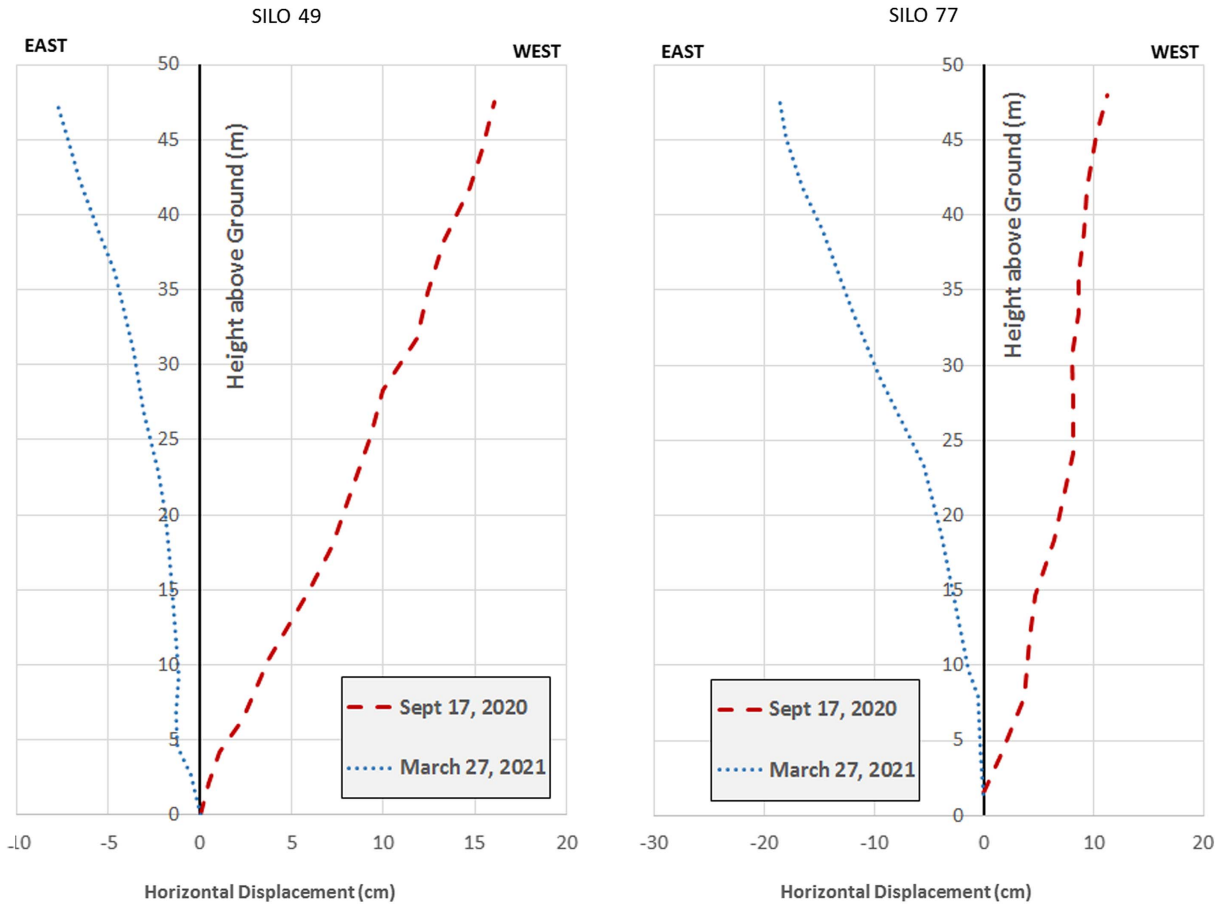


**Fig. 9.** Representative horizontal movements for Silos 49 and 77 (Northern Block) showing postblast readings on Sept 17, 2020, and readings on March 27, 2021. (Base scans courtesy of Amann Engineering.)

(1975–1990), building construction was affected by poor building code design provisions and lack of material quality control (Salameh et al. 2016). Despite Lebanon being seismically active, during that era most of the buildings in Beirut were designed to resist gravity loads only, with little or no consideration to lateral resistance. Seismic provisions in building codes were introduced in the 1990s, but were not strictly enforced until 2013 (with the publication of the second edition of the Lebanese earthquake standards; LIBNOR 2013). Still, structures built after 1990 can generally be considered modern. Table 1 summarizes the evolution of the building stock in Beirut, namely typical structural systems, design and construction quality, and building heights.

This section describes GEER data collection and results. Collection consisted of in-person building inspections conducted shortly after the blast and street-view imagery about two months after. Reconnaissance was strongly affected by the global COVID-19 pandemic, which curtailed international travel, as well as by US-Lebanon shipping restrictions, which limited our ability to import reconnaissance equipment [e.g., from the National Science Foundation (NSF) Natural Hazards Reconnaissance Facility] to assist in the work.

### *In-Person Building Inspections*

The American University of Beirut Maroun Semaan Faculty of Engineering and Architecture (AUB-MSFEA) set up an emergency hotline and engineering dispatch center for Beirut residents and businesses concerned about the structural safety of buildings following the explosion. Teams of engineers visually assessed buildings, provided advice on imminent dangers from structural, nonstructural, or falling hazards, and recommended possible mitigation measures.

Inspections included visual assessments of exteriors and (in most cases) interiors. The team photographed building façades and structural and/or nonstructural damage visible inside or outside of buildings. They completed an assessment survey form for each structure visited. The assessment form was based on the Applied Technology Council's ATC-20 (ATC 1995) and ATC-45 (ATC 2004) rapid and detailed evaluation safety assessments, with modifications to suit the local setting as detailed in Sadek et al. (2021a). An important distinction between the GEER building inspections and those by OEA is that GEER's documentation more specifically delineated damage to structural (i.e., load-bearing) versus nonstructural elements, which conforms with protocols widely used in post-earthquake reconnaissance. Some of the damage recorded in these surveys may have preceded the explosion (e.g., shrapnel during the Lebanese civil war, prior settlement of foundations, corrosion due to water leakage), but were still reported. They were distinguished from damage due to the explosion whenever possible through visual identification or when reported as such by residents.

Fig. 12 shows the locations of 172 buildings inspected during this effort, most located within 2 km of the blast.

### *Street-View Photographs*

Street-view high-resolution photograph surveys were performed on October 8 and 15, 2020. The purpose was to document the


**Fig. 10.** Aerial views of ground zero (Hangar 12) prior to July 31, 2020, and immediately following explosion (August 4, 2020). (Base map © 2021 Google Earth; Image © 2021 Maxar Technologies.)

damaging effects of the blast for a large number of structures, albeit with less information per structure than in-person inspections could provide.

We originally attempted to use street-view equipment owned and maintained by the Natural Hazards Reconnaissance Facility in the US, but this was ultimately deemed unworkable. As a result, we instead used a commercially available GoPro Fusion camera mounted on the roof of a car. The camera was used in a mode that allows manual control of the number of images taken in order to ensure optimal coverage with a practical number of images. All photos were geo-tagged (i.e., latitude and longitude), and the azimuth of the photograph (i.e., the direction pointed toward) was recorded. Fig. 12 shows the routes taken by the camera-mounted car. This method of reconnaissance could be undertaken safely given the public health challenges present at that time in Beirut. All of the images (2,100 in total) and the related metadata collected in this survey, were uploaded to mapillary.com and have been archived as described in the section "Data and Resources."

### *Structural Damage Assessment*

In this subsection, we describe how the reconnaissance data were interpreted to provide damage classifications, and we present several examples of damage. The interpretation of spatial patterns in the data is presented in a subsequent section.

Structural damage was classified via in-person inspections using a system adapted from Bray and Stewart (2000) and European Macroscale 1998 (Grünthal 1998). Damage indices ranged from D0 (no observed damage) to D5 (complete collapse of a floor or the entire structure), as provided in Table 2. The index descriptions were specific to this study.

Classifications were assigned to each of the 172 buildings that were inspected in-person by the GEER/AUB-MSFEA team. An additional 10 buildings were classified as having heavy damage (D3–D5) based on the 360° photos described previously. In total, 182 buildings were classified: 73 stone masonry (SM) bearing-wall buildings (for some of which concrete frames had been added within an existing floor or to build upper levels) and 109 reinforced concrete (RC) buildings. These buildings were located at blast distances of 0.6 to 4.4 km, with most being within 2 km.

Fig. 13 shows RC and SM buildings with variable levels of damage. Figs. 13(a and b) show two modern high-rise RC structures with a D2 damage classification. These buildings, located ~700 m from the explosion, sustained moderate damage to

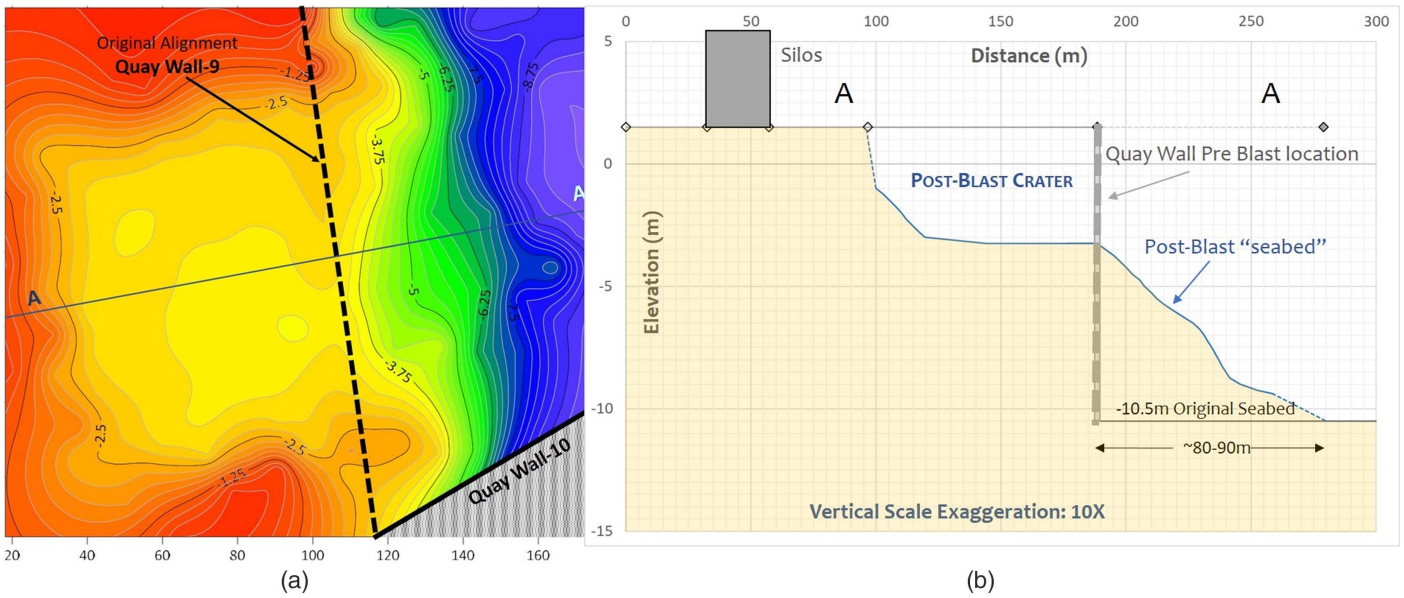


**Fig. 11.** (a) Water depths from bathymetric survey conducted on August 8, 2020; and (b) west-east cross-section through center of crater. (Bathymetric data courtesy of Lebanese army.)

**Table 1.** Characteristics of Beirut building stock

| Year | Structural system | Likely design and construction quality[a] | Height[b] |
|---|---|---|---|
| Before 1935 | Stone masonry bearing walls[c] | GLD; good | Low-rise |
| 1935–1955 | Stone masonry bearing walls[c] | GLD; good | Low-rise |
| | Mixed stone masonry bearing walls and reinforced concrete frames | GLD; good | Low-rise; mid-rise |
| 1955–1975 | Reinforced concrete frames | GLD; good | Mid-rise |
| 1975–1990 | Reinforced concrete frames | GLD; poor | Mid-rise |
| 1990–2005 | Reinforced concrete frames and walls | GLD or SD; good | Mid-rise; high-rise |
| After 2005 | Reinforced concrete frames and walls | SD; good | Mid-rise; high-rise |

Source: Adapted from Salameh et al. (2016).
[a]GLD = gravity-load design; and SD = seismic design.
[b]Low-rise: up to 4 stories; mid-rise: 5 to 12 stories; and high-rise: more than 12 stories.
[c]Wood, reinforced concrete, or steel slabs.

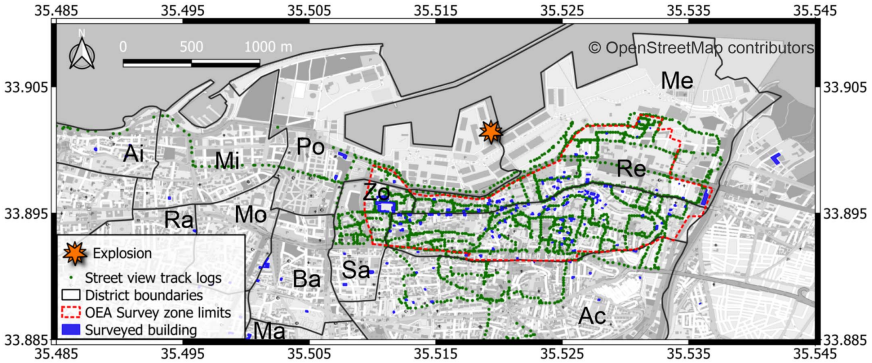


**Fig. 12.** Locations of buildings subject to in-person inspections and tracks of 360° photo surveys from GEER reconnaissance. (Data from Sadek et al. 2021a; Base map © OpenStreetMap Contributors.)

nonstructural components (e.g., cladding and false ceilings) but no apparent structural damage. Fig. 13(c) shows an SM building that sustained heavy structural damage (D3), namely significant cracking of its exterior bearing walls, failure of its façade arches and balconies, and partial collapse of its roof. Finally, Figs. 13(d–f) show two partially collapsed (D4) and one totally collapsed (D5) SM buildings, respectively. Sadek et al. (2021a) provides additional examples. The damage classification of all 182 buildings is available in the published data set (Sadek et al. 2021b).

Some of the buildings inspected by OEA (2020) were assigned a structural damage classification and subsequently used in the analysis of spatial damage patterns. These were buildings reported by OEA (2020) to be partially or totally collapsed and those with partial or total collapse of a roof or slab; they were given a damage classification of D4 or D5. The other buildings have not yet received structural damage classifications because the available information from those inspections does not include photographs and other details needed to support a classification.

### *Façade Damage Assessment*

Using the ~2,100 street view photos, we classified façade damage to building openings (windows, doors, and frames). This assessment was performed remotely by four investigators. Consistency in the damage assessment process was ensured by cross-checking results in regular meetings designed to minimize between-analyst discrepancies. The number of inspected façades was greater than the number of analyzed photos because one photo typically contained multiple façades belonging to different buildings. The damage assessment was performed using QGIS, and the results were stored in a geodatabase (details in "Data and Resources"). Façade damage was classified according to the damage levels provided in Table 3 (newly developed for this GEER deployment). For each building façade inspected, the geodatabase contained damage classes, azimuth, break/blow-out rates (for Damage classes 1 and 2), and comments on reconstruction activities in the period between the explosion and the dates when the photos were taken.

Fig. 14 shows façades assigned to Damage classes Wxx-1, where damage was mainly related to broken windows [Fig. 14(a)], Wxx-2, where windows were broken and frames were damaged [Fig. 14(b)], and Wxx-3, the highest façade damage level, where there was complete blow-out of panels within building frames [Fig. 14(c)]. The photos shown were taken in different districts of Beirut.

### *Damage Pattern Interpretation*

Fig. 15 shows maps of the spatial distributions of structural and façade damage. The damage is mapped by shading buildings with classified damage (per Tables 2 or 3). Unshaded buildings are in the AUB-BUL database, but lack postevent damage classifications. As shown in Fig. 15, the city was radially divided into three subareas denoted western, central and eastern to examine possible azimuthal differences in damage distribution.

Because the structural damage data was relatively sparse, damage patterns could be more easily seen in the façade data [Fig. 15(b)]. Of the analyzed façades, 5,388 were classified as Wxx-0, 1,158 as Wxx-1, 759 as Wxx-2, and 1,920 as Wxx-3. Fig. 15(b) shows a clear fringe area separating undamaged zones (Wxx-0) from zones with some damage (Wxx > 1). This fringe zone was located at variable distances from the explosion: ~1.5 km in the western area, ~0.7–0.9 km in the central area,

**Table 2.** Structural damage classifications

| Structural elements | Damage summary | Damage descriptors by typology: Sandstone bearing-wall buildings | Damage descriptors by typology: RC buildings |
|---|---|---|---|
| *D0* | | *No damage* | |
| *D1* | | *Light damage* | |
| Load-bearing structural elements | No damage | Hairline cracks in a few walls<br>Fall of small pieces of plaster only | Fine cracks in plaster over frame elements or in wall bases |
| Nonstructural elements[a] | Minor damage/cracking | — | Fine cracks in partition and infill walls |
| *D2* | | *Moderate damage* | |
| Load-bearing structural elements | Minor damage/cracking (insignificant displacement across cracks) | Cracks in many walls; Fall of large pieces of plaster | Cracks in columns, beams, and structural walls |
| Nonstructural elements | Moderate damage/cracking | Moderate damage to façade arches, balconies; Moderate damage to roofs, ceilings | Moderate cracks in partition walls; infill walls; Fall of brittle cladding, plaster; Falling mortar from joints of wall panels; Moderate to heavy damage to false ceilings |
| *D3* | | *Heavy damage* | |
| Load-bearing structural elements | Significant damage (cracking with significant deformations across cracks) but no collapse | Large, extensive cracks in most walls<br>Tilting or separation of bearing walls | Cracks in columns, beam column joints of frames at base and joints of coupled walls<br>Spalling of concrete cover<br>Buckling of steel rebars |
| Nonstructural elements | Heavy damage/cracking | Failure of individual nonstructural elements<br>Heavy damage, failure of façade arches, balconies<br>Heavy damage to roof, ceilings | Large cracks in partition and infill walls<br>Failure of individual infill panels<br>Heavy damage to false ceilings |
| *D4* | | *Partial structural collapse* | |
| Load-bearing structural elements | Collapse of portion of building. | Serious failure of walls<br>Partial structural failure of roofs, floors | Large cracks in structural elements<br>Compression failure of concrete<br>Fracture of rebars; bond failure of beam rebars<br>Tilting of columns<br>Collapse of a few columns or single upper floor |
| Nonstructural elements | Very heavy damage/cracking | — | — |
| *D5* | | *Full structural collapse* | |
| | | Complete collapse of floor or entire structure | |

Source: Adapted from Bray and Stewart (2000); and Grünthal (1998).
Note: Classification based on main structure; appendages (e.g., additional room built with masonry blocks on roof) not considered in classification.
[a]Nonstructural elements include partition walls, false ceilings, external cladding, balconies, façade arches, exclude glazing, door, window frames, contents, and equipment.

and ~1.2 km in the eastern area. This analysis suggested a nonsymmetric façade damage spatial distribution, possibly related to the damping effect of tall buildings/structures and/or the different levels of structural vulnerability in different districts of the city.

As described in the section "Building Impacts", Beirut buildings are predominantly of SM and RC construction. The ones most damaged by the blast (D3, D4, and D5) were sandstone bearing-wall structures and older (gravity load–designed) RC buildings. Modern RC structures located close to the blast suffered damage mostly to nonstructural elements. Fig. 16 illustrates the distribution of damage classes D0 to D5 for SM and RC structures based on the in-person survey data only. The data showed that the SM buildings generally suffered more damage than the RC buildings.

Fig. 17 shows the distribution of damage classes among the assessed structures and façades for the entire city as well as the three subareas shown in Fig. 15. Fig. 17(a) focuses on structural damage and considers two data populations. The "unbiased" structural sample consisted of the 182 structures subject to in-person and 360° photo inspection (as described in "Structural Damage Assessment" section). The second population (the supplemented sample) added 243 collapsed or partially collapsed buildings (D4–D5) identified by OEA (2020). Those collapsed structures are a subset of those indicated as having "full or partial collapse" in Fig. 1, after removing "collapses" that involved only balconies and not primary load-bearing systems, based on information in OEA (2020). These additional D4–D5 buildings biased the data set toward higher average damage ratings, in that it did not representatively sample structures across all performance levels. The charts in Fig. 17(a) indicate that the most severe structural damage effects were in the central and eastern subareas. The apparently severe damage in the eastern subarea was likely influenced by most of the OEA evaluations having been performed in that part of the city.

Fig. 17(b) shows the façade damage distributions. Contrary to the structural damage information, these data indicated that the western subarea experienced the most impact relative to the other subareas. Because of the much larger sample size in the façade data set and the aforementioned biased sampling of structural damage, trends in the façade data set were considered to more accurately represent the spatial distribution of blast impacts in the city. The apparently greater façade damage in the western subarea of the city may have resulted from a concentration of office buildings in that region, which were slower to be repaired than residential structures


**Fig. 13.** Buildings with variable levels of blast damage: (a and b) RC structures with moderate nonstructural damage (e.g., cladding, false ceilings) but no apparent structural damage (D2); (c) stone masonry building with heavy damage (D3) including significant cracking of exterior bearing walls, failure of façade arches and balconies, and partial roof collapse; (d and e) partially collapsed stone masonry buildings (D4) (image reprinted from Sadek et al. 2021a); and (f) totally collapsed stone masonry building (D5). [Images (a and c) by Rami Rizk; images (b, e, and f) by Mayssa Dabaghi.]

**Table 3.** Façade damage to building openings (windows, doors, frames); classifications dependent on azimuth *xx*, defined as horizontal angle from north to line orthogonal to façade

| Façade impact | Description |
|---|---|
| Wxx-0 | No observable effects on windows or doors |
| Wxx-1-yy | Some windows broken, frames generally intact (yy% break rate); doors remain in place |
| Wxx-2-zz | Some window and door/door frames blown out (zz% blow-out rate) |
| Wxx-3 | Nearly complete blow-out of windows, doors, window/door frames |

that predominated in other subareas. It is also possible that directional patterns in the damage may have been associated with shielding from tall buildings, although such effects can only be speculated upon at the present time and are not discussed further here.

Fig. 18 shows variations in damage ratings (represented by box and whisker plots) with distance from the explosion for both façade and structural data sets. In the box and whisker plots, the two ends of the boxes represent the upper quartile (25% of the data are greater than this value) and lower quartile (25% of the data are smaller than this value), respectively; the vertical line inside the box represents the median value; and the two whiskers represent the minimum and maximum values within that category. For both data sets, the most severe damage ratings occurred at the closest distances, with less severe damage (on average) occurring at greater distances. These trends were also observed within each of the three subareas, although the distance trend was strongest in the west subarea. This was likely because most of the structures and façades assessed in this area were along the coastline with a direct line of sight to the explosion. As a consequence, there were fewer complicating factors (shielding, etc.) that might have impeded the natural attenuation of damage with distance.

### *Comparison with Damage Proxy Maps*

Following disasters, the Advanced Rapid Imaging and Analysis (ARIA) team at the Jet Propulsion Laboratory and the Space Geodesy group at the Earth Observatory of Singapore produce synthetic aperture radar (SAR)-based damage proxy maps (DPMs). Such


**Fig. 14.** Façade damage levels: (a) Wxx-1, damage to windows only; (b) Wxx-2, damage to windows and frames; and (c) Wxx-3, complete blow-out of panels within building frames.

maps are produced using pre- and postdisaster radar data. The technique used to produce DPMs is based on differences in phase statistics of microwaves returning to a satellite (e.g., Fielding et al. 2005; Yun et al. 2011, 2015).

Following the August 4, 2020, Beirut explosion, a DPM was produced using SAR data from the Copernicus Sentinel-1 satellites. This DPM was generated by comparing pre- and postexplosion SAR scenes acquired from four different tracks. The satellite tracks viewed Beirut from the west (two) and the east (two), with look angles from vertical ranging between 31° and 44°. The map used 12 preevent and 2 postevent SAR scenes between May 1, 2020, and September 1, 2020. The map covered an area of $13 \times 16$ km (Fig. 19). Each pixel was about $10 \times 10$ m. Shaded pixels represent zones where there was significant change in radar wave scattering at the reflectors (i.e., ground surface or buildings), which may indicate damage from the stressing event.

Fig. 20 is a box and whisker plot highlighting how DPM correlates with structural damage; DPM in this plot has been converted to a numerical index between 0 and 1.0. This index corresponds the shading on maps over the index range of 0.75–1.0, as shown in the plot (the index range of 0–0.75 produces no map shading). The undamaged structures consistently occurred at index values <0.75, and the damaged structures occurred at index values >0.75. Among structures with damage (Classes D1 to D5), the DPM index was highest for structures with full or partial collapse (D4–D5) (median >0.9) and was approximately the same (median of about 0.8) for structures with damage states D1 to D3. This indicates that the DPM index distinguishes among damage levels at a high level (no damage, damage, collapse) but does not distinguish among damage levels short of collapse.

Fig. 21 is a box and whisker plot highlighting how the DPM correlated with façade damage. The undamaged state (Wxx-0) had a median DPM index near the lower limit of shading (about 0.75). Among structures with façade damage, the DPM index could not distinguish between damage levels Wxx-1 and Wxx-2 (median DPM index of about 0.8), whereas the strongest level of damage (Wxx-3) had a clearly higher median DPM index of 0.9.

## Summary and Conclusions

In this paper, we presented data compiled from reconnaissance of the effects of the August 4, 2020, explosion on Beirut infrastructure. We described impacts on the Port of Beirut where the explosion occurred and on buildings in the city up to a distance of approximately 4 km. This paper was derived from a report by GEER (Sadek et al. 2021a), with some updates when additional information became available.

For the Port, impacts were documented for Quay Wall 9, which collapsed as part of a flow slide in which a crater formed at the blast site and presumably liquefied fill material flowed into the adjacent

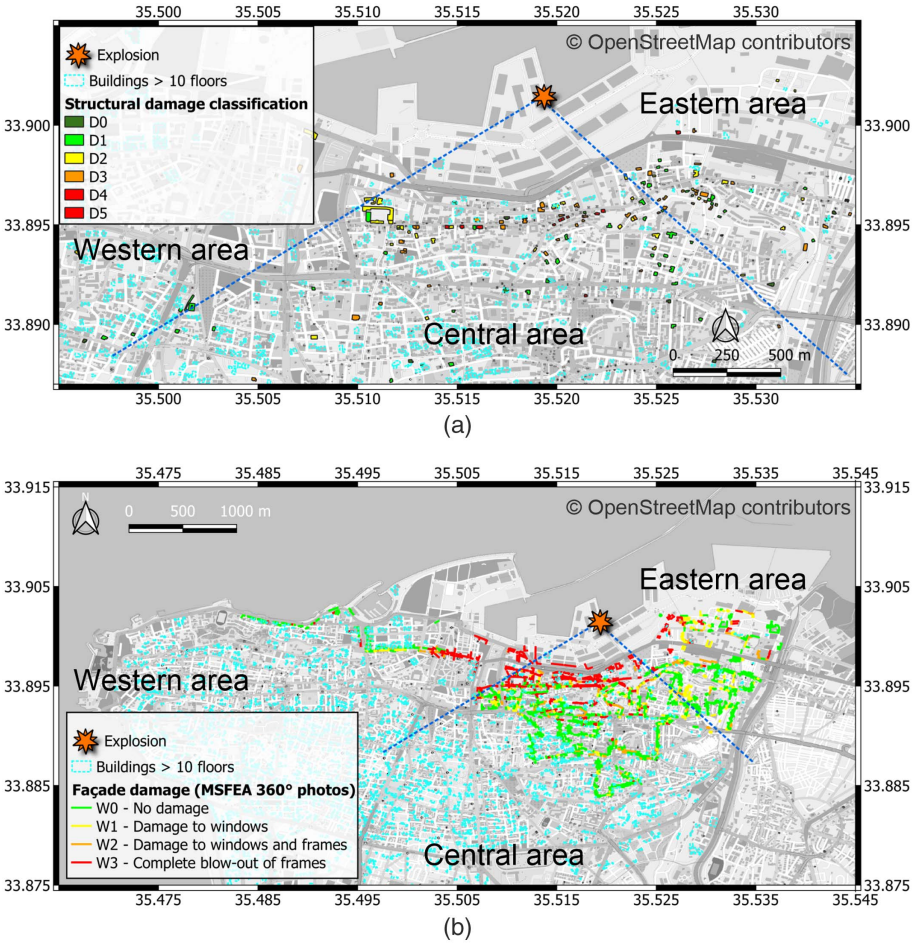


**Fig. 15.** (a) Structural; and (b) façade damage distribution maps. Radial lines are for analysis of azimuthal effects on damage patterns. (Base maps © OpenStreetMap Contributors.)

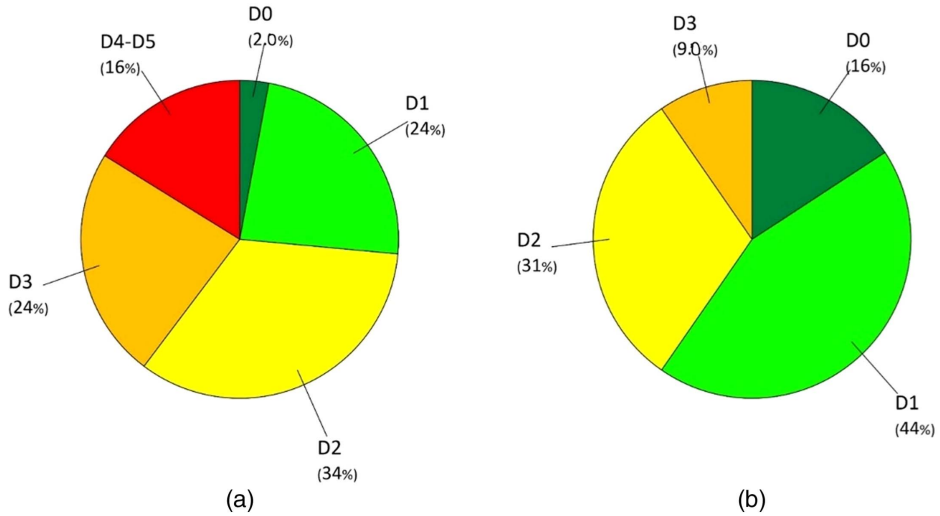


**Fig. 16.** Distribution of damage classes in (a) stone masonry buildings (68); and (b) reinforced concrete buildings (114).

Basin 3. We also described impacts on a series of grain silos located as close as 50 m from the blast source. Most of the silos were lost as a result of blast impact, although a row of silos (furthest from the blast) survived. That row of silos initially tilted toward the west by up to ~0.5%, and in the 9 months since the blast some of them experienced a reversal in the direction of tilt to a maximum ~0.5% toward the east (net slope reversal ~1%).

In portions of Beirut west, south, and east of the explosion, different levels of building damage occurred, varying from full collapse to no structural or façade damage at blast distances under

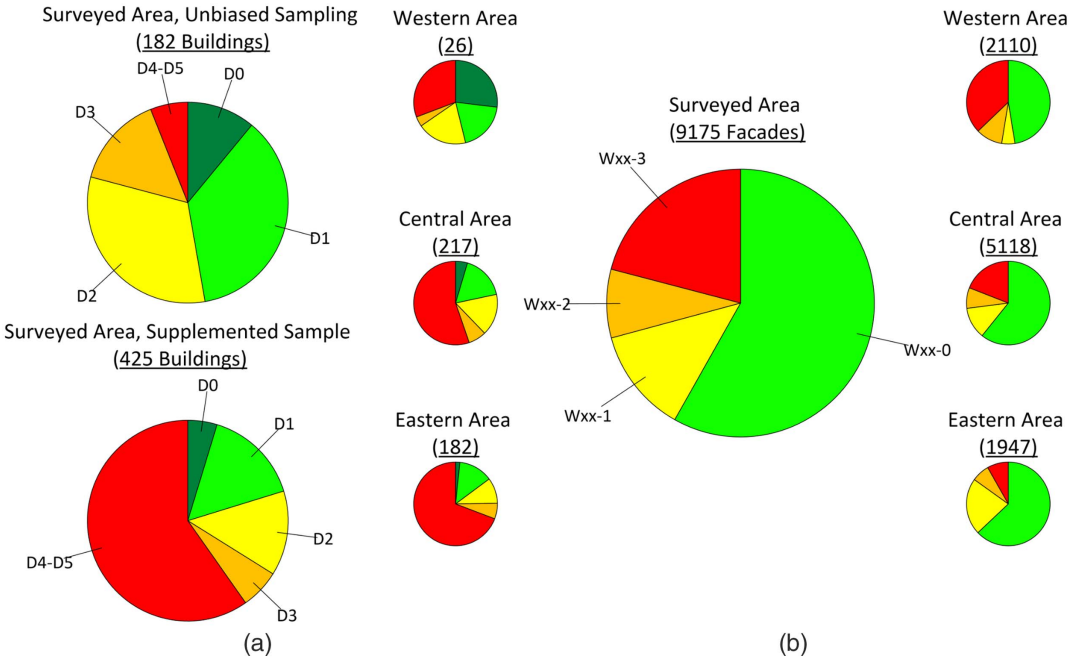


**Fig. 17.** (a) Structural; and (b) façade damage distributions in all surveyed areas and subareas.

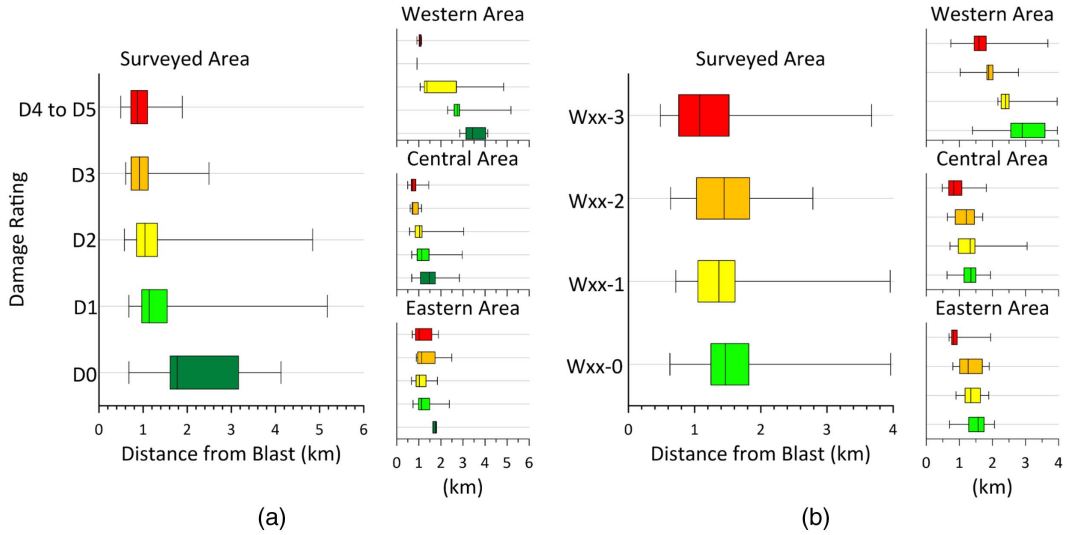


**Fig. 18.** (a) Structural; and (b) façade damage variations with distance in all surveyed areas and subareas.

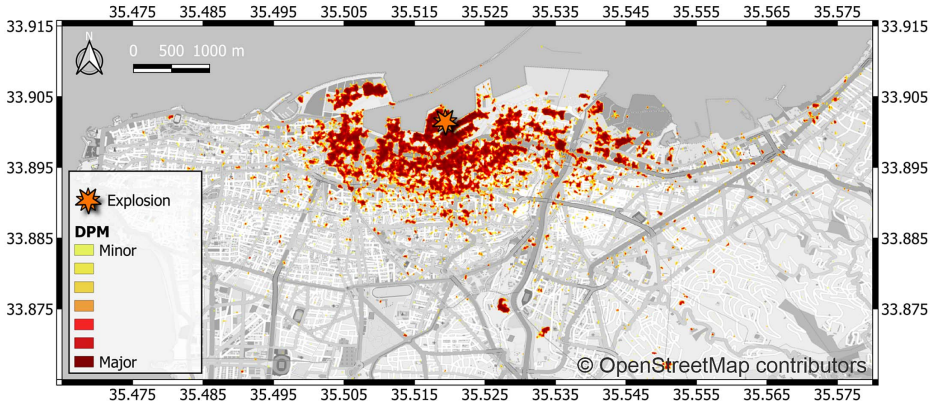


**Fig. 19.** DPM produced following blast. (Data from NASA-JPL; Base map © OpenStreetMap Contributors.)



Nat. Hazards Rev., 2022, 23(2): 04022008

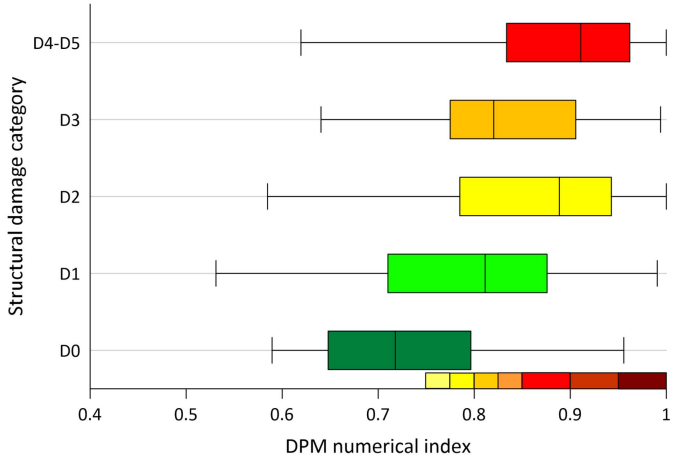


**Fig. 20.** Relationship between numerical index of DPM (0–1) and structural damage categories.

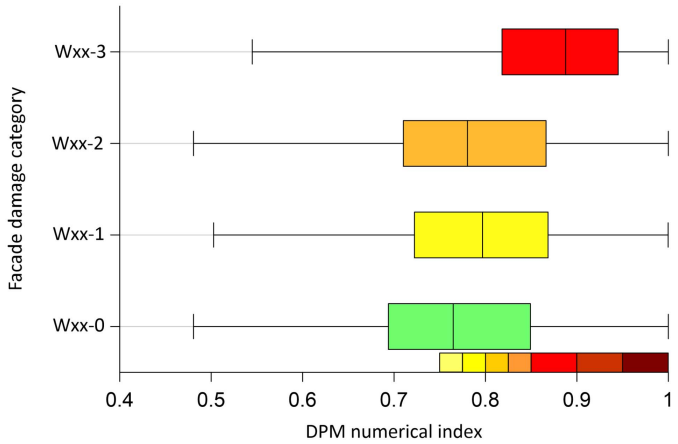


**Fig. 21.** Relationship between numerical index of DPM (0–1) and façade damage categories.

4 km. Notably, sporadic damage due to the blast extended to much farther distances in the form of broken windows and doors, impacting some facilities at the Beirut Rafic Hariri International Airport 8 km away from the explosion. We documented both structural impacts and façade damage (mainly to windows and doors) as derived from structure-specific inspections and interpretation of street-view imagery. We showed that the attenuation of damage with distance from the source was azimuth-dependent, decaying relatively rapidly in the central and eastern subareas of the city (areas of relatively dense urbanization with many buildings) and more gradually to the west (where the blast pressure pulse was able to travel relatively far before encountering buildings).

The data collected from postevent reconnaissance (Sadek et al. 2021b) can be used in future research on a variety of topics, which include

- Analysis of the blast impact on the silo structures to see if the observed collapses, and survivals, of particular silos are predictable. The tilt of the silo foundations and its time variation is also of interest.
- Analysis of the apparent flow slide to derive residual strengths, and pairing this with penetration resistance data for the remaining portions of the Port fill (Fig. 5).
- Based on inspections and imagery from OEA (2020), expansion of the inventory of buildings with classified structural damage and updates of the analyses using this data set.
- Study of factors affecting damage distributions in Beirut using dynamic simulations of the blast pulse through the city, particularly shielding of portions of the city by tall intervening structures.
- Further analysis of DPM effectiveness regarding the damage from the blast and tracking of recovery as buildings are repaired.

## Data Availability Statement

Some or all data, models, or code generated or used during the study are available in a repository online in accordance with funder data retention policies. The damage proxy map used in this study was retrieved from the NASA-JPL ARIA event page at https://aria-share.jpl.nasa.gov/20200804-Beirut_Blast/ (last accessed June 2021). Locations of 360° photos taken in October 2020, detailed structural damage assessment information for 172 buildings based on in-person inspection within a month of the explosion, exterior structural damage assessment information for 10 buildings based on 360° photos taken in October 2020, and façade damage assessment data based on using 360° photos taken in October 2020 are available in DesignSafe (Sadek et al. 2021b; https://doi.org/10.1007/s00193-020-00970-z). All 360° photos are available in Mapillary (https://www.mapillary.com/app/?lat=33.90191008577155&lng=35.49106252100046&z=14.512378027628445) and Beirut Recovery websites (https://beirutrecovery.org/). For both websites, photos can be visualized after selecting user: aubmsfea in the main menu. Building polygons are from the Beirut Urban Lab (available at: https://beirut-built-environment-database-bul-aub.hub.arcgis.com/).

## Acknowledgments

The GEER Association is supported in part by the National Science Foundation through the Geotechnical Engineering Program under Grant No. CMMI-1826118. Any opinions, findings, and conclusions or recommendations expressed in this material are those of the authors and do not necessarily reflect the views of the NSF. Any use of trade, firm, or product names is for descriptive purposes only and does not imply endorsement by the US Government. The GEER Association is made possible by the vision and support of the NSF Geotechnical Engineering Program Directors Dr. Richard Fragaszy and the late Dr. Cliff Astill. GEER members also donate their time, talent, and resources to collect time-sensitive field observations of the effects of extreme events. Part of the research was sponsored by the NASA Earth Science Disasters Program (Grant No. 18-DISASTER18-0034) and performed in collaboration with Sang-Ho Yun of the Jet Propulsion Laboratory, California Institute of Technology. Many people contributed to the reconnaissance reported here. They are listed in the Acknowledgments section of Sadek et al. (2021a). We would like to call special attention to Mr. Emmanuel Durand (Amann Engineering, Geneva) for generously sharing his time and monitoring data. We appreciate the constructive comments provided by the anonymous reviewers of this paper.

## References

Al-Hasjj, S., A. H. Mokdad, and A. Kazzi. 2021. "Beirut explosion aftermath: Lessons and guidelines." *Emergency Med. J.* 38: 938–939. https://doi.org/10.1136/emermed-2020-210880.

Aouad, C., W. Chemissany, P. Mazzali, Y. Temsah, and A. Jahami. 2020. "Beirut explosion: Energy yield from the fireball time evolution in the first 230 milliseconds." Preprint, submitted October 5, 2020. https://arxiv.org/abs/2010.13537.

ATC (Applied Technology Council). 1995. *Addendum to the ATC-20 post-earthquake building safety evaluation procedures*. Rep. No. ATC-20-2. Redwood City, CA: ATC.

ATC (Applied Technology Council). 2004. *Field manual: Safety evaluation of buildings after windstorms and floods*. Rep. No. ATC-45. Redwood City, CA: ATC.

Beirut OEA (Order of Engineers and Architects). 2020. *Beirut port explosion of Aug 04 2020: Buildings final structural assessment report*. Beirut: OEA.

Bray, J. D., and J. P. Stewart. 2000. "Damage patterns and foundation performance in Adapazari." *Earthquake Spectra* 8 (16A): 163–189.

Dar Group. 2020. "Beirut after August 4: Damages and insights." Accessed July 1, 2021. https://dar.com/insights/details/beirut-after-august-4-damages-and-insights.

Dechy, N., T. Bourdeaux, N. Ayrault, M.-A. Kordek, and J. C. LeCoze. 2004. "First lessons of the Toulouse ammonium nitrate disaster, 21st September 2001, AZF plant, France." *J. Hazard. Mater.* 111 (1–3): 131–138. https://doi.org/10.1016/j.jhazmat.2004.02.039.

Diaz, J. S. 2020. "Explosion analysis from images: Trinity and Beirut." Preprint, submitted September 11, 2020. https://arxiv.org/abs/2009.05674.

Fielding, E. J., M. Talebian, P. A. Rosen, H. Nazari, A. Jackson, M. Ghorashi, and R. Walker. 2005. "Surface ruptures and building damage of the 2003 Bam, Iran, earthquake mapped by satellite synthetic aperture radar interferometric correlation." *J. Geophys. Res.* 110 (B3). https://doi.org/10.1029/2004JB003299.

Grünthal, G. 1998. *European Macroseismic Scale 1998 (EMS-98)*. Working Group Macroseismic Scales. Luxembourg: Conseil de l'Europe, Cahiers du Centre Européen de Géodynamique et de Séismologie.

Ismail, S., W. Raphael, and E. Durand. 2021. "Case study of the Beirut port explosion using 3D laser scan and non-linear finite element model." *Res. Eng. Mater.* 7 (4): 551–577. https://doi.org/10.17515/resm2021.286st0428.

LIBNOR (Lebanese Standards Institution). 2013. *Earthquake loads: General rules*. Dekwaneh, Lebanon: LIBNOR.

LRC (Lebanese Red Cross). 2020. "Disaster management sector Beirut port explosion response assessment results (MSNA, DANA) as of August 24, 2020." Accessed July 1, 2021. https://reliefweb.int/sites/reliefweb.int/files/resources/dm-rp-msna-dana-200825.pdf.

Ministry of Public Works and Transport. 1970. *Silos of the port of Beirut–construction pamphlet*. Beirut: Directorate General of Land and Maritime Transport.

Nemer, T. S. 2021. "The Beirut port explosion: A geoscience perspective." *Seismol. Res. Lett.* 92 (4): 2093–2098. https://doi.org/10.1785/0220210051.

New York Times. 2020. "How a massive bomb came together in Beirut's Port." Accessed July 1, 2021. https://www.nytimes.com/interactive/2020/09/09/world/middleeast/beirut-explosion.html.

OEA (Order of Engineers and Architects). 2020. "Beirut explosion: Buildings' weekly structural assessment report." Accessed July 1, 2021. https://www.oea.org.lb/Library/Files/news/2020/sep%202020/building%20Weekly%20Report%203.pdf?fbclid=IwAR0fH4X7Ksp0GdbQMHDypWPmgTY25FFX2RFruy5rJmOyjR3KVWLBIOahT-VU.

Pilger, C., P. Hupe, P. Gaebler, A. Kalia, F. Schneider, A. Steinberg, H. Sudhaus, and L. Ceranna. 2021. "Yield estimation of the 2020 Beirut explosion using open access waveform and remote sensing data." *Sci. Rep.* 11: 14144. https://doi.org/10.1038/s41598-021-93690-y.

Rathje, E. M., C. Dawson, J. E. Padgett, J.-P. Pinelli, D. Stanzione, A. Adair, P. Arduino, S. J. Brandenberg, T. Cockerill, and M. Esteva. 2017. "DesignSafe: New cyberinfrastructure for natural hazards engineering." *Nat. Hazards Rev.* 18 (3): 06017001. https://doi.org/10.1061/(ASCE)NH.1527-6996.0000246.

Rigby, S. E., T. J. Lodge, S. Alotaibi, A. D. Barr, S. D. Clarke, G. S. Langdon, and A. Tyas. 2020. "Preliminary yield estimation of the 2020 Beirut explosion using video footage from social media." *Shock Waves* 30 (6): 671–675. https://doi.org/10.1007/s00193-020-00970-z.

Sadek, S., M. Dabaghi, I. Elhajj, P. Zimmaro, Y. M. A. Hashash, S.-H. Yun, T. M. O'Donnell, and J. P. Stewart. 2021a. *Engineering impacts of the August 4, 2020 Port of Beirut, Lebanon explosion*. GEER Rep. No. 070. Canaan, CT: Geotechnical Extreme Events Reconnaissance Association.

Sadek, S., M. Dabaghi, P. Zimmaro, Y. M. A. Hashash, T. O'Donnell, and J. P. Stewart. 2021b. "*In person damage assessment and 360° photo collection and analysis, in GEER—August 4, 2020 Beirut port explosion*." *DesignSafe-CI*, March 12, 2021. https://doi.org/10.17603/ds2-rh78-ak38.

Salameh, C., B. Guillier, J. Harb, C. Cornou, P. Y. Bard, C. Voisin, and A. Mariscal. 2016. "Seismic response of Beirut (Lebanon) buildings: Instrumental results from ambient vibrations." *Bull. Earthquake Eng.* 14 (10): 2705–2730.

SARAID (Search and Rescue Assistance in Disasters). 2020. "Post-deployment report: Beirut explosion 6th–12th August, 2020." Accessed October 27, 2021. www.saraid.org.

Temsah, Y., A. Jahami, and C. Aouad. 2021. "Silos structural response to blast loading." *Eng. Struct.* 243 (Sep): 112671. https://doi.org/10.1016/j.engstruct.2021.112671.

Valsamos, G., M. Larcher, and F. Casadei. 2021. "Beirut explosion 2020: A case study for a large-scale urban blast simulation." *Saf. Sci.* 137 (May): 105190. https://doi.org/10.1016/j.ssci.2021.105190.

World Bank Group. 2020. *Beirut rapid damage and needs assessment*. Washington, DC: World Bank Group.

Yu, G.-D., Y. Wang, L. Zheng, J. Huang, J.-L. Li, L.-Z. Gong, R. Chen, W. Li, J. Huang, and Y.-S. Duh. 2021. "Comprehensive study on the catastrophic explosion of ammonium nitrate stored in the warehouse of Beirut port." *Process Saf. Environ. Prot.* 152 (Aug): 201–219. https://doi.org/10.1016/j.psep.2021.05.030.

Yun, S., E. J. Fielding, M. Simons, P. Rosen, S. Owen, and F. Webb. 2011. "Damage proxy map of February 2011 M 6.3 Christchurch earthquake using InSAR coherence." In *Proc., 8th Int. Workshop on Advances in the Science and Applications of SAR Interferometry*. Frascati, Italy: European Space Agency—European Space Research Institute.

Yun, S.-H., et al. 2015. "Rapid damage mapping for the 2015 M w 7.8 Gorkha earthquake using synthetic aperture radar data from COSMO–SkyMed and ALOS-2 Satellites." *Seismol. Res. Lett.* 86 (6): 1549–1556. https://doi.org/10.1785/0220150152.

Zhang, X., Y. Ding, and Y. Shi. 2021. "Numerical simulation of far-field blast loads arising from large TNT equivalent explosives." *J. Loss Prev. Process Ind.* 70 (May): 104432. https://doi.org/10.1016/j.jlp.2021.104432.